Chem

CellPress

Article

pH-Directed Aggregation to Control Photoconductivity in Self-Assembled Perylene Bisimides

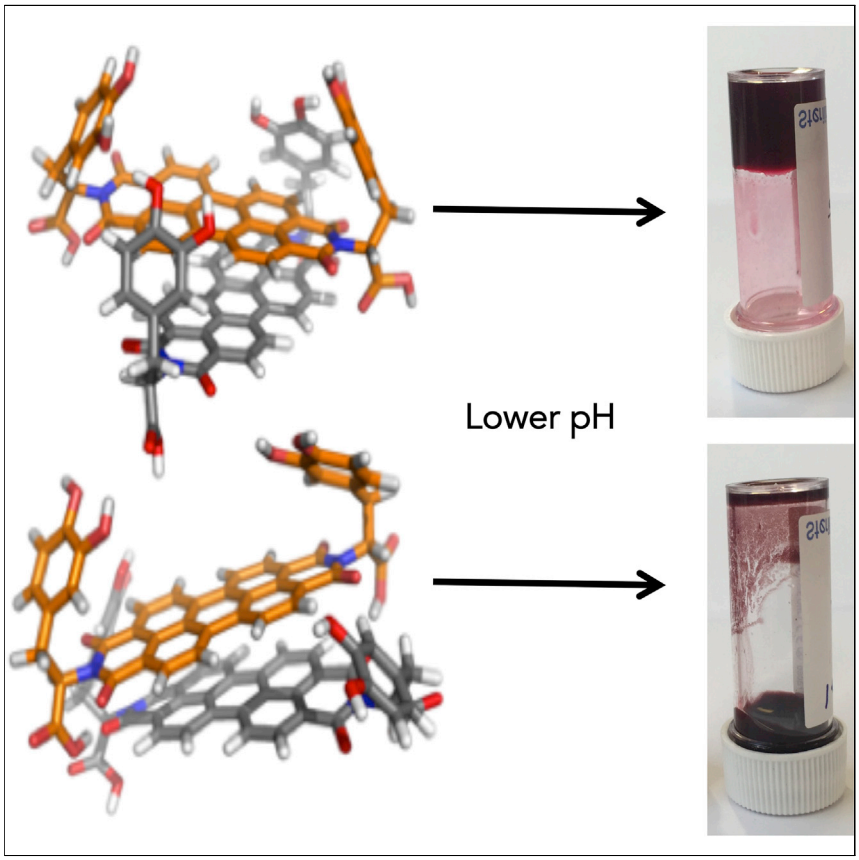

The aggregate type and self-assembly of a perylene bisimide n-type organic semiconductor can be controlled by subtle variations in the solution conditions. The different aggregates form photoconductive films with very different properties.

Emily R. Draper, Benjamin J. Greeves, Michael Barrow, Ralf Schweins, Martijn A. Zwijnenburg, Dave J. Adams

dave.adams@glasgow.ac.uk

HIGHLIGHTS

The type of molecular aggregation can be controlled by pH

Inter-change between aggregates is reversible but on different timescales

The different aggregates give materials with different properties

The process of self-assembly can be fine-tuned for controlling properties

Draper et al., Chem 2, 716–731
May 11, 2017
http://dx.doi.org/10.1016/j.chempr.2017.03.022

7 AFFORDABLE AND CLEAN ENERGY

CrossMark

Chem

CellPress

Article

pH-Directed Aggregation to Control Photoconductivity in Self-Assembled Perylene Bisimides

Emily R. Draper,[1,2] Benjamin J. Greeves,[2] Michael Barrow,[2] Ralf Schweins,[3] Martijn A. Zwijnenburg,[4] and Dave J. Adams[1,2,5,*]

SUMMARY

Perylene bisimides (PBIs) are one example of useful π-conjugated molecules that can be used in optoelectronic devices as n-type materials with strong visible light absorption. PBIs can self-assemble into a range of structures, but it is rare to be able to control the packing such that the same PBI can form either H-type or J-type aggregates. This is important because the conductivity pathways and optoelectronic properties are directly affected by this packing. Here, we show that we can control the packing of a single PBI functionalized with an amino acid by a subtle change in pH. Under one set of conditions, H-type aggregates form a gel when the pH is decreased. At a slightly different set of starting conditions, J-type aggregates are formed, but they cannot form a gel when the pH is lowered. We show that films formed from the self-assembled structures have very different photoconductive properties.

INTRODUCTION

Self-assembly of aromatic organic molecules can be used to prepare materials for a range of optoelectronic and light-driven applications.[1–4] There are many potential advantages here, including the relatively low cost of the molecules and the potential to fine-tune the properties of the materials by subtle variations in molecular structure and assembly method. When used in a device, a key issue is that the device performance will be driven by the type of aggregates formed. Thus, it is critical to be able to control the aggregate size and shape, the molecular packing in the aggregate, and the interactions between the aggregates. Self-assembly can be used as an effective approach to direct the aggregation, because small changes in the weak forces holding the molecules together can have a profound effect on the aggregate structure. However, it is often difficult to predict, understand, and rationalize the outcome of the self-assembly process.

For self-assembled aromatic molecules, the aggregation is driven by the π interactions between molecules, as well as other weak interactions built into the molecule. Generally, one-dimensional aggregates such as fibers, wires, or tubes are desired, and hence interactions that drive aggregation in one dimension are required. On aggregation, π-rich systems generally form either H-type or J-type aggregates, defined by whether aggregation leads to a blue or red shift in the absorption maximum of the UV-visible (UV-vis) spectrum, respectively. These spectral differences arise from how the molecules are packed, even if the link between spectra and packing motifs is sometimes more complicated than suggested by the textbook model,[5] which importantly links directly to their expected efficiency in optoelectronic devices.

The Bigger Picture

Self-assembly is a useful way of organizing aromatic molecules for light-driven applications such as solar cells and photocatalytic H_2 evolution. However, to be effective, we need to control the type of aggregates that are formed when the molecules are stacked. It is critical to be able to line the molecules up in the most effective way such that the conductive pathways are optimal. This is normally difficult to control, so it is often necessary to use environmentally unfriendly solvents or annealing steps to drive toward the desired structure. It is also possible to change the molecular structure to drive toward the desired type of stacking. This, however, requires exhaustive synthesis, and there are often limited design rules. Ideally, it would be possible to direct the self-assembly down multiple pathways by rational design for a molecule with the desired optoelectronic properties. Here, we present such an approach for a self-assembled n-type organic semiconductor.

Perylene bisimides (PBIs, also called perylene diimides or PDIs) are robust, versatile dyes that can be functionalized with many different groups.[6,7] These functional groups can lead to PBIs with a variety of properties.[8,9] One of these properties is the aggregation state adopted by the relatively insoluble PBIs in solution, where either H or J aggregates can be formed. In general, bulkier substituents on the PBIs, especially in the bay position, are more likely to lead to J aggregation. Subtle changes in the side groups can result in a PBI that prefers to assemble as an H aggregate instead of a J aggregate.[10–13] For example, Ghosh et al.[10] have described close structural analogs that prefer to stack as either H or J aggregates depending on the substituents.

H and J aggregates are expected to strongly differ in their (photo)conducting properties.[14,15] From a theoretical perspective, the charge carrier mobility and exciton diffusion rate in self-assembled materials are expected to depend on the relative orientation of the constituting molecules and hence the type of packing. This has been verified experimentally. For example, previous work from the literature on self-assembled PBI materials has found that J aggregates display facile exciton transport,[16,17] whereas the diffusion length in H aggregates is much shorter.[18] Because improving both the exciton and charge carrier mobility is expected to increase the photoconductivity of a material, controlling the self-assembly process appears to be a good strategy for developing better photoconductors.

However, as mentioned, in most cases, the assembly of a PBI leads to the formation of a specific type of aggregate. Changes in the type of self-assembled morphology are possible with changes in the solvent conditions, but this generally occurs on the nanoscale, and the molecular packing is not significantly changed. Although there are numerous examples where the morphology can be affected, changing the type of molecular packing usually requires the synthesis of a new molecule, which is clearly a time-consuming exercise. A significantly more attractive approach would be to induce a single PBI to adopt different molecular packing.

However, only a very small number of examples have been described where a single PBI can adopt either aggregation state in solution, for example, by changing the solvent polarity[19] or by adding a binding ligand.[20] Changes in the color of thin films of a PBI on exposure to warm solvent vapor, indicative in a shift from H to J aggregation, have been reported.[21] Thermal annealing can also be used to switch between H and J aggregates in a thin film.[22] Overall, switching between aggregation states for a single molecule (i.e., without a chemical change) is thus rare.

Here, we show that we can use subtle changes in solution pH as a means of adjusting the molecular packing of a PBI functionalized at the imide positions with L-DOPA (L-3,4-dihydroxyphenylalanine; Figure 1A). This PBI-DOPA has been described previously and self-assembled by initial dissolution in DMSO followed by dilution with water.[23] Changes in fluorescence were observed on addition of different metal salts or surfactants. We have found that different types of aggregate can be formed from this PBI depending on the pH of the solution (and hence the degree of deprotonation, **A1** and **A2**; Figure 1A). The two aggregate types have significantly different behavior.

RESULTS AND DISCUSSION

A range of PBIs that are functionalized at the imide position with an amino acid have been prepared.[24–32] We have shown that a number of these form viscous solutions at

[1]School of Chemistry, WESTChem, University of Glasgow, Glasgow G12 8QQ, UK

[2]Department of Chemistry, University of Liverpool, Crown Street, Liverpool L69 7ZD, UK

[3]Institut Laue-Langevin, Large Scale Structures Group, 71 Avenue des Martyrs, CS 20156, F-38042 Grenoble CEDEX 9, France

[4]Department of Chemistry, University College London, 20 Gordon Street, London WC1H 0AJ, UK

[5]Lead Contact

*Correspondence: dave.adams@glasgow.ac.uk

http://dx.doi.org/10.1016/j.chempr.2017.03.022

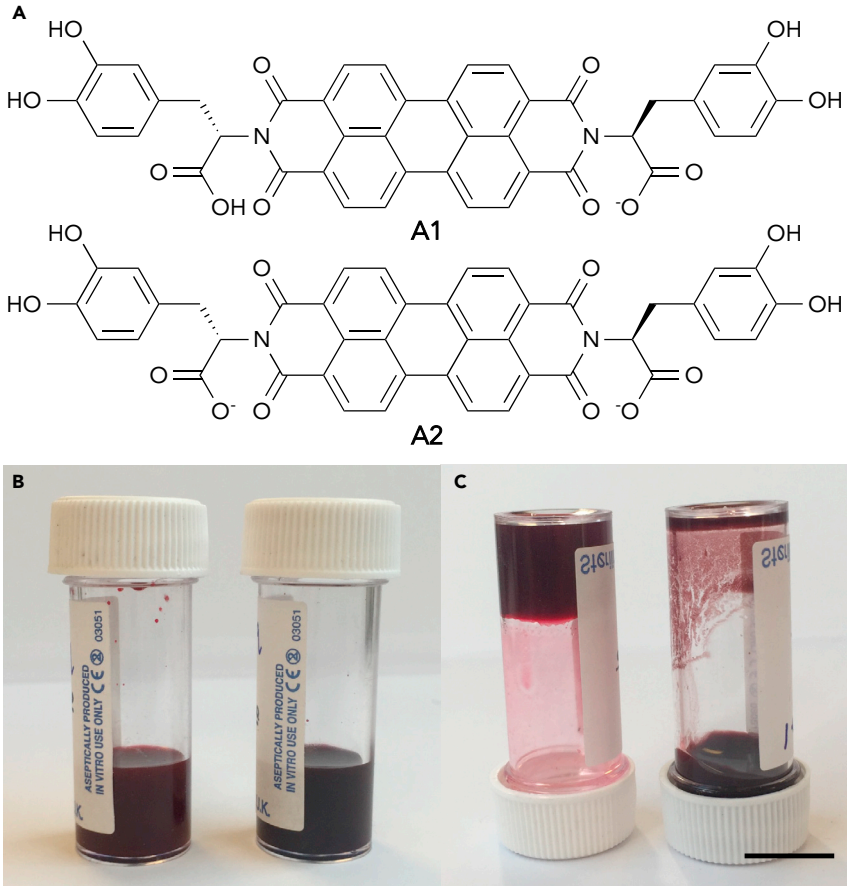

Figure 1. The Perylene Bisimide Used in This Study and Its Behavior at Different pH

(A) Chemical structure of PBI-DOPA at different degrees of deprotonation **A1** and **A2**.

(B) Photographs of **A2** formed at pH 8.2 (left) and of **A1** formed at pH 6.7 (right).

(C) Photographs of the solution of **A2** upon a decrease in pH to 3.3 (left) and of the solution of **A1** upon a decrease in pH to 3.3 (right). The scale bar represents 1.5 cm.

elevated pH, where the C terminus is deprotonated; gels form as the pH is decreased. The PBI-DOPA used here was prepared as described previously.[23] This PBI has two apparent pK_a values, as determined by a titration with HCl from high pH. pH 6.7 is the pH of the highest apparent pK_a (we refer to these as apparent pK_a values on the basis of work on related systems, where it has been shown that this is most likely the pK_a of an aggregate and not the molecule[33–35]). On the addition of 1 molar equiv of sodium hydroxide to a suspension of this PBI at a concentration of 5 mg/mL in water, a dark purple solution at pH 6.7 was formed (**A1**; Figures 1A and 1B). A pink solution at pH 8.2 was formed when 2 molar equiv of base were added (**A2**; Figures 1A and 1B).

A1 and **A2** were characterized on the basis of their UV-vis absorption and fluorescence spectra. It is clear from these data that solutions of **A1** and **A2** contain different types of aggregate. In agreement with the previous reports on PBI-DOPA,[23] **A2** showed a UV-vis spectrum that had absorption maxima at 510 and 550 nm, which is very similar to the UV-vis absorption spectrum reported for solutions of PBI substituted with simple amino acids.[24] In contrast, the UV-vis absorption spectrum of **A1** showed the presence of an extra peak at 620 nm (Figure 2A), not normally seen for amino-acid-substituted

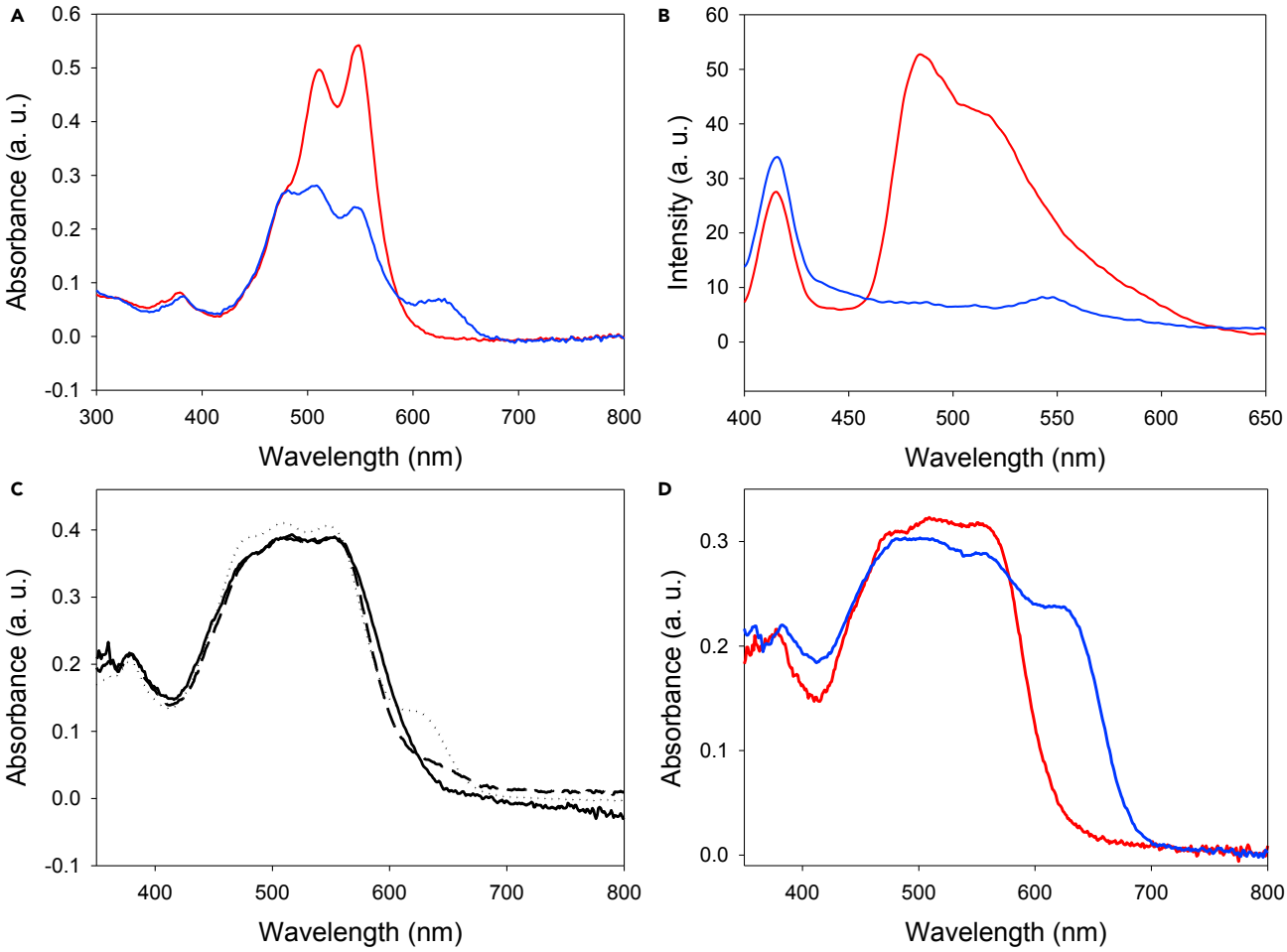

Figure 2. UV-Vis and Fluorescence Data for A1 and A2

(A) UV-vis absorption spectra for the solution of **A2** (red data) and the solution of **A1** (blue data) at a concentration of 0.039 mg/mL.

(B) Emission fluorescence spectra excited at 385 nm for solutions of **A1** (blue data) and **A2** (red data) at a concentration of 0.039 mg/mL.

(C) UV-vis absorption spectra at 5 mg/mL of **A1** after the addition of 1 equiv of NaOH (solid line), 1 equiv HCl after 20 hr (dashed line), and 1 equiv HCl after 24 hr (dotted line).

(D) Solid-state UV-vis absorption spectra of thin films formed from a solution of **A2** (red data) and from a solution of **A1** (blue data). More UV-vis absorption spectra can be found in Figures S2–S4 and S10.

PBIs. It is tempting to label the spectra of **A1** and **A2** as the result of H and J aggregation, respectively. The peak at 620 nm is, for example, normally assigned to the formation of a J aggregate in PBI-based organogels.[10,11,19,36] However, the relative intensity of the peak at 620 nm in comparison with the peaks at 510 and 550 nm is lower than for some examples in the literature.[10] The solution of **A1** is also much less fluorescent than that of **A2**; at least the simplest model of H and J aggregates would suggest that J aggregates should be more fluorescent than H aggregates.

We hypothesized that the 620 nm peak could have such a low intensity because this solution contains both types of aggregates. However, by carrying out a slow titration, we found that although both aggregates had the same first apparent pK_a, the solution of **A1** and **A2** had different second apparent pK_a values. The solution of **A2** had a second apparent pK_a at 5.7, whereas the solution of **A1** had a second apparent pK_a at 5.4 (Figure S1 and Supplemental Information). The perhaps

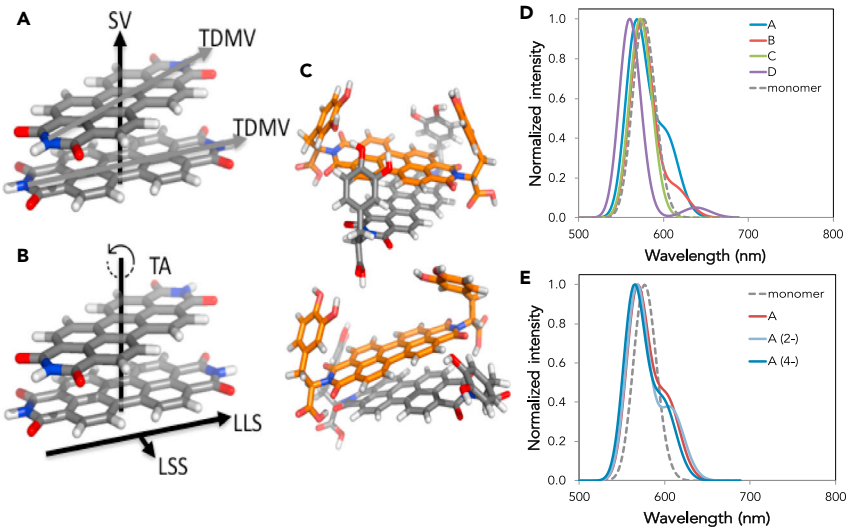

Figure 3. A Microscopic Picture of the Molecular Packing

(A) Illustration of the possible orientations of the molecular transition dipole moment vectors (TDMVs) and the stacking vector (SV).

(B) Illustration of the main structural degrees of freedom in a packing: twist angle (TA), lateral shift along the long axis of the PBI core (LLS), and lateral shift along the short axis (LSS).

(C) The DFT optimized structures of, from top to bottom, dimer models A and D (note that one PBI-DOPA in each dimer has been colored orange for clarity).

(D) TD-DFT (wB97x) predicted spectra of the different dimer models.

(E) TD-DFT (wB97x) predicted spectra of deprotonated dimer model A in different deprotonation states. The predicted TD-DFT spectra, as discussed in the Supplemental Information, include a rigid red shift of 0.7 eV.

surprisingly high apparent pK_a values have been attributed to the aggregation state and correlates with the high pK_a values that have been seen for related molecules.[33–35] The two distinct apparent pK_a values for the different aggregates show that a solution of **A1** does not contain a mixture of aggregates of **A1** and **A2**. This was further confirmed by UV-vis absorption spectroscopy; dilutions of both solutions showed that all the peaks decreased at a similar rate (Figure S2 and Supplemental Information), again suggesting the presence of only one structure in each solution. The two different solutions were also added to each other. The resulting UV-vis spectrum was found to be a simple addition of the two spectra from the solutions of **A1** and **A2** (Figure S3 and Supplemental Information). This shows that the two species are self-sorted in solution when mixed.[10]

Interestingly, when 1 molar equiv of sodium hydroxide was added to the solution of **A1**, the peak at 620 nm immediately disappeared from the UV-vis absorption spectrum, which became identical to that of the solution of **A2** (Figure 3A). When the pH was lowered again by the addition of 1 molar equiv of HCl, initially the UV-vis absorption spectrum looked very similar to that of **A2**. The peak at 620 nm reappeared after approximately 20 hr and reached the original intensity of the solution of **A1** after 7 days (Figure 3A). The same slow appearance of the peak at 620 nm occurred when 1 molar equiv of HCl was added to a freshly prepared solution of **A2** (Figure S4 and Supplemental Information). This suggests that although the formation of the structure with the peak at 620 nm is the thermodynamic product when only one of the carboxylic acids is deprotonated, time is needed for molecular re-orientation to occur to allow the change from the other packing that does not give rise to this

peak. We assume that the relatively fast kinetics of forming **A2** and slow kinetics of forming **A1** are related to the anisotropy of **A1** and a preferred relative orientation of the deprotonated carboxylic acid groups in the agglomerate.

To explain the spectra described above, we need to understand the molecular packing in (solutions of) **A1** and **A2** to link the packing and spectra. Traditionally, when molecular aggregates are discussed from a theoretical perspective, the focus is generally on cases where the transition dipole moment vectors (TDMVs) of the individual molecules (Figure 3A, in the case of PBIs orientated along the long axis of the PBI core for the lowest-energy singlet excitation) all point in the same direction, and the only degree of freedom is the orientation of these TDMVs in relation to the stacking vector (SV; Figure 3A), the vector that connects the centers of mass of the molecules in the stack. If the TDMVs and SV point in the same direction, Kasha's quasi-classical exciton model[37] predicts that a J aggregate is formed, with a red-shifted absorption spectrum in relation to that of the non-aggregated molecule, and if the TDMVs and SV are orthogonal, an H aggregate with a blue-shifted absorption spectrum is formed. However, in addition to the fact that the coupling between molecules can be more complicated than assumed by Kasha,[5] the molecules in a stack also do not all need to be orientated in the same direction. As can be seen from Figure 3B, the molecules can be rotated or translated in relation to one another. Indeed, previous computational work on unsubstituted PBIs terminated with N–H bonds[38–40] (which are held together by π-π interactions alone) and PBIs substituted with simple amino acids, such as valine, (which can also form hydrogen bonds between the carboxylic acid protons of the amino acids and carbonyl oxygen atoms of the PBI cores)[41] found that in the likely structures of the aggregates formed, each molecule was rotated with respect to the molecule below and above it by ~30°–35° (the twist angle from Figure 3B), a rotated-stack aggregate. One of the implications of a non-zero twist angle based on Kasha's exciton model is that, instead of a bright excitation due to the constructive addition of transition moments and a completely dark excitation due to destructive addition, both of the aggregate excitations should have a finite intensity.

PBIs functionalized with more complex amino acids, such as the PBI-DOPA studied here, are capable of forming multiple hydrogen bonds, also involving the hydroxyl groups on the substituents, and hence can potentially be directed to structures other than those preferred on the basis of maximizing the π-π interaction and hydrogen bonds involving the carboxylic acid protons alone. To investigate whether other such structures are indeed likely to form and whether their existence would explain the spectral features observed, we computationally explored the different ways PBI-DOPA can pack. Similar to previous computational work,[41–43] for reasons of computational tractability in this exploration, we focus on a dimer of PBI-DOPA. Such a tentative exploration of the energy landscape of a PBI-DOPA dimer, consisting of an initial conformer search using empirical potentials and subsequent dispersion-corrected density functional theory (DFT) optimization of low-energy conformers using Grimme's PBEh-3c approach[42] (see Supplemental Information), shows that PBI-DOPA, among other things, can indeed form rotated-stack aggregates with much larger twist angles of 45°–70° and some degree of lateral shift, as well as structures where the molecules lie parallel to one another but are stacked in a staircase-like fashion. In line with our hypothesis, both classes of structures involve hydrogen bonds between the L-DOPA hydroxyl groups. Moreover, this exploration of the energy landscape also suggests that both classes of structures lie low in energy and for neutral PBI-DOPA are significantly more stable than dimer models of small-angle rotated-stack agglomerates, analogous to the structures found with simpler amino

acid substituents discussed above. Calculations on deprotonated structures, discussed in more detail in the Supplemental Information, suggest that this energetic picture does not significantly change upon deprotonation, other than a destabilization of the staircase structures. Although they are tentative and only consider PBI dimers, these calculations clearly suggest that the presence of hydroxyl groups on the amino acid substituent facilitates the formation of molecular arrangements not seen for simpler substituents.

To correctly describe charge-transfer excitations, spectra calculated with time-dependent DFT and the long-range corrected wB97x[43] and CAM-B3LYP[44] functionals on the optimized geometries of the dimer models of PBI-DOPA agglomerates can be seen in Figures 3D and S14. The rotated stacks with a larger twist angle (A and B) are predicted to have a red-shifted shoulder that is not present in the staircase-like stacking model (C) and the rotated stacks with a small twist angle (D). The latter, however, has a low-intensity broad peak that is even further red-shifted but that might be hard to observe experimentally. Figure 3E shows the predicted spectra of A after deprotonation of one and two carboxylic acid groups per molecule, modeling the conditions under which **A1** and **A2** were prepared. Clearly, deprotonation is predicted to have only a minor effect on the spectra. Although the dimer models are only approximations of the structures present in experiments and although we neglect vibronic coupling, in line with suggestions from previous model Hamiltonian calculations by Hestand et al.,[5] it appears that the rotated-stack structures with large twist angles can explain the presence of a J-like red-shifted shoulder seen in the experimental solution (Figure 2A) and solid-state (Figure 2D) UV-vis absorption spectra of **A2**, and why such features would not have been observed for PBIs substituted with simpler amino acids. We see no evidence of changes in the thermodynamically preferred structure or spectra upon deprotonation in our calculations, suggesting that the experimentally observed switch with pH explicitly involves either the hydrated sodium counter-ions or larger length scales, both of which cannot be readily incorporated in our computational model.

Finally, as discussed in the introduction, it is clear that although we can assign aggregates as either H-type or J-type on the basis of their UV-vis absorption spectra, this does not mean that the underlying structure of such aggregates necessarily corresponds to the archetypal textbook pictures. Dimer model D has approximately orthogonal TDMVs and SVs, but because of the large twist angle, it still has a J-like feature in the absorption spectrum. Moreover, although we have not performed TD-DFT excited-state relaxation calculations to predict the fluorescence spectra of the dimers, the fact that **A2** is fluorescent and **A1** is not also challenges the classic picture of H and J aggregates.

The change in molecular packing has a profound effect on the self-assembly. Viscosity measurements for the two solutions suggest that the solution of **A1** contains worm-like micelles, as shown by shear-thinning behavior. The solution of **A2** has the same viscosity as water; this could indicate the presence of spherical structures or that the aggregates are simply very small (Figure S5 and Supplemental Information). To probe this further, we used small-angle neutron scattering (SANS). The data and fits are shown in Figure 4. It is clear immediately that the solution of **A1** scatters more strongly than that of **A2**. The higher degree of charge on **A2**, resulting in increased solubility and hence a higher on-off rate from the self-assembled structures means the structures are less persistent. The data for the solution of **A2** can be fitted well to an absolute power law with a gradient of 2.83 ± 0.01. We interpret this as above; structures are present, but there is a low residence time for the

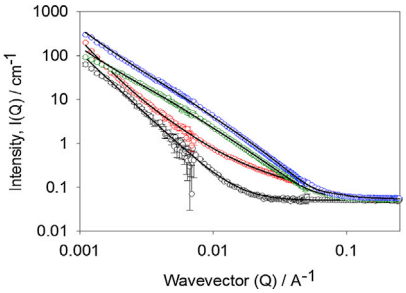

Figure 4. SANS Data and Fits for A1 and A2
Green data are for a solution of **A1**. Blue data are for the suspension of **A1** at low pH. Black data are for a solution of **A2**. Red data are for a gel of **A2** at low pH. In all cases, the black lines are the fits to the data as described in the text.

molecules in the self-assembled aggregate. The data for the solution for **A1** were fitted best to a flexible cylinder model combined with a power law component; the low Q region is sensitive to the fractal scattering from the network structure. We fit the data by fixing the Kuhn length to a number of different values and minimizing the residuals. The best fit was found to be a cylinder of radius 5.65 $\pm$ 0.46 nm, a Kuhn length of 5.3 $\pm$ 2.7 nm, and a length of over 920.5 $\pm$ 73 nm. The power law was 2.11 $\pm$ 0.01. These data agree with the viscosity data above, implying that long, worm-like structures are present in solutions of **A1**.

The solutions of **A1** and **A2** also show different gelation abilities. When the pH was lowered to 3.3 with glucono-δ-lactone (GdL), which hydrolyzes slowly in water to gluconic acid,[45,46] the solution of **A2** formed a self-supporting gel (Figure 1C) with a storage modulus (G′) of ~380 Pa and G″ of ~35 Pa (Figure S6A and Supplemental Information), which broke at a strain of 8% (Figure S6B and Supplemental Information). These data are typical for low-molecular-weight gels formed from PBIs functionalized with amino acids.[24] Indeed, scanning electron microscopy (SEM) shows that the sample contains a fibrous network at this point (Figure S7 and Supplemental Information). The SANS data are also consistent with a fibrous network; the scattering increases significantly from that of the solution of **A2** and changes shape (Figure 4). The data are now best fitted to the flexible cylinder combined with an absolute power law. Here, the data fit to a cylinder with a radius of 2.53 $\pm$ 0.14 nm, a Kuhn length of 26.97 $\pm$ 2.09 nm, and a length of 269.3 $\pm$ 74.1 nm. The power law was found to fit to 3.19 $\pm$ 0.07. These data are consistent with a cross-linked network of thin fibers. However, decreasing the pH of a solution of **A1** to 3.3 with GdL resulted instead in precipitation rather than gelation. The scattering data could still be fitted well to a flexible cylinder combined with an absolute power law. Again, we achieved the fit by fixing the Kuhn length to a number of values and optimizing on the basis of the residuals. A power law of 2.29 $\pm$ 0.04 was found, very similar to that for **A1** at higher pH. The radius was also found to be very similar (5.81 $\pm$ 0.26 nm). The Kuhn length and length could be fitted well across a number of values strongly affecting the radius or power law, and the best fit was for a length of 538.9 $\pm$ 30.2 nm and a Kuhn length of 10.0 $\pm$ 0.79 nm. This fit implies that long anisotropic structures are present in solution. Large irregular aggregates can be seen on SEM (Figure S8 and Supplemental Information), which can be an effect of drying or could imply that the scattering data are sensitive only to the primary assembled structures. Decreasing the pH of **A2** with 1 equiv of HCl to that of a solution of **A1** and then immediately adding GdL still resulted in the formation of a gel, showing that the different gelation results are not simply an effect of the initial pH before GdL addition. However, allowing this solution to stand for a week after the addition of HCl (and hence allowing the packing to change to that shown by **A1**; see discussion above) and then adding GdL resulted in a precipitate. This

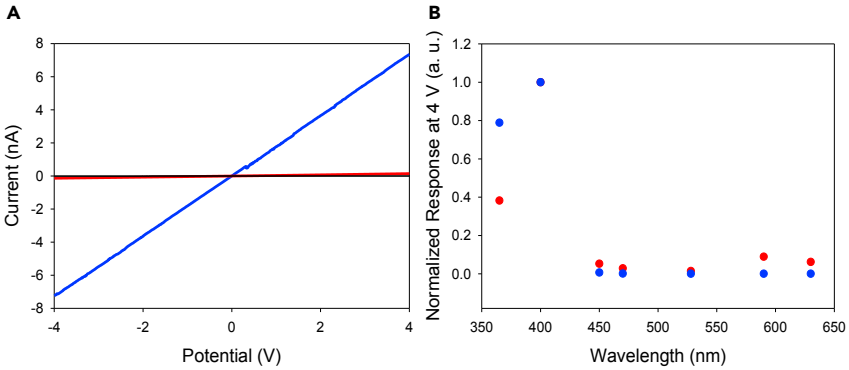

Figure 5. Photoconductivity Measurements

(A) Current-voltage curve of the thin films during irradiation with 400 nm LED. Red data are for the dried film formed from **A2**, blue data are for **A1**, and black data are for the corresponding dark measurements.

(B) Normalized photoresponse of the thin films at 4 V at different wavelengths of light. Blue data are for **A1**, and red data are for **A2**. The data for **A1** and **A2** at 400 nm overlap are normalized at this wavelength. Non-normalized data are shown in Figure S12A.

slow evolution between the structures initially adopted by **A2** and that of **A1** is in agreement with our UV-vis data described above.

As discussed above, changes in the type of molecular aggregation should give rise to differences in photoconductivity. We have previously shown that a number of PBIs functionalized at the imide position with an amino acid can be used to form photoconductive films.[24,47] We prepared the films by drying solutions of the self-assembled PBIs in air. The conductivity arises from the formation of the radical anion when the films are irradiated with a 365 nm LED, which is surprisingly stable in air.[24,41,47–49] In these papers, we proved the formation of the radical anion by electron paramagnetic resonance and spectroelectrochemistry and also postulated that the amino acid substituent can act as an electron donor, although the amount of decomposition was below the detectable limit of analytical tools such as nuclear magnetic resonance.

Here, when a solution of either **A1** or **A2** was dried to form a thin film, both kept their J-type or H-type aggregate character, as shown by the solid UV-vis absorption spectra (Figure 2B). Powder X-ray diffraction (pXRD) data on the two dried films show that the two samples are essentially amorphous (Figure S9 and Supplemental Information). The dried films of both **A1** and **A2** show the presence of the radical anion when irradiated with UV light, as shown by the formation of new peaks in the UV-vis absorption spectra at 730 nm (Figures S10A and S10B; Supplemental Information).[50]

The photoconductivity under illumination for films formed from either **A1** or **A2** was measured and compared. Although films of both aggregates were photoconductive, the film formed from **A1** was considerably more photoresponsive than that formed from the solution of **A2** (Figure 5A). We stress that this is based on many repeat films and not an isolated example. The absolute thicknesses of the films were very similar (typically 2.4 μm for **A1** and 2.9 μm for **A2**), and the films were continuous (Figure S11 and Supplemental Information). Because the absolute conductivity depends on the intensity of the irradiation source and the degree of alignment of structures in the film, we do not directly compare the magnitude of the response to that in previous work.[24,47,51,52] Instead, we focus on the wavelength

response. Interestingly, both samples were most responsive when illuminated at 400 nm with some response at 450 nm. This is unlike similar materials that were most responsive at 365 nm (Figure 5B).[24] We hypothesize that this shift in the response into the visible region is due to the self-doping nature of the L-DOPA.[48,53,54] To prove that it is not simply an effect of morphology (i.e., the presence of worm-like micelles that give rise to the higher photoconductivity for the dried solution of **A1**), the pH of a solution of **A2** was lowered to 6.5. As expected from the discussion above, the UV-vis absorption spectrum remained similar to that of **A2**. However, viscosity data indicated that worm-like micelles were now present in solution as a result of the lower pH (Figure S12A and Supplemental Information). This shows that the morphology of the self-assembled aggregate can be independent of the molecular packing. An aliquot of this solution was then allowed to dry. The UV-vis absorption spectrum for this dried film was consistent with that of the solution, showing that the packing was not changed on drying. The wavelength dependence measurements on this film were only very weakly photoresponsive at all wavelengths (Figure S12B and Supplemental Information). This shows that the photoconductivity is dependent on molecular-level packing rather than the morphology of the self-assembled structure.

Overall, it is clear from the calculations that, as hypothesized above, the use of these more complicated substituents, which allow for additional intermolecular interactions, leads to new packing motives not seen for simpler substituents and the appearance of new J-like spectral features, in line with those observed experimentally. These features arise from differences in the degree of twisting of the PBIs in relation to one another, and these differences in the twist can lead to profound differences in the photoconductivity. The packing suggested by the dimers for **A1** (Figure 3) is clearly much more effective than that for **A2**.

To conclude, we have shown here a rare example of a PBI that is able to reversibly switch between aggregation types after a subtle change in pH. The two aggregates show different properties, such that the J-like aggregate is significantly more photoresponsive than the H-like aggregate. The H-like aggregate is able to form gels when the pH is decreased, whereas the J-like aggregate cannot. These data again illustrate that the process by which gelling is carried out is critical.[55] In addition, our data show that the presence of the hydroxyl groups on the substituents at the imide position on the PBI opens up the possibility of hydrogen bonding with the carbonyl groups, and therefore there is the potential to form extra supramolecular interactions. These interactions mean that, compared with PBIs substituted with simpler groups, the PBIs reported here enable different molecular packing. Importantly, these new packing possibilities lie at lower energies than conventional stacks. Interpretation of the packing with simple models based on classic pictures of H- and J-type packing is difficult.

Systems such as those described here are often under non-equilibrium conditions. This implies that the self-assembly should be highly dependent on how aggregation is induced, and hence it should be possible for a single molecule to adopt different molecular packing by subtle changes in the assembly process. This should then allow very different material properties to be adopted from a single molecule, provided that one can robustly control the self-assembly. In line with this hypothesis, we have shown here that it is possible to adjust the packing such that the macroscopic photoconductivity can be controlled by careful control of the initial solution pH. This work opens up new opportunities for photoconductive materials and shows the potential of including more complex substituents at the imide position to control molecular packing.

EXPERIMENTAL PROCEDURES

Synthesis of PBI-DOPA

PBI-DOPA was synthesized as previously reported.[23] All materials used for synthesis were purchased from Sigma-Aldrich and used as received. Distilled water was used throughout.

Preparation of H- and J-type Aggregates of PBI-DOPA

All solutions were prepared at 5 mg/mL of gelator in water. For the solutions of **A2**, the sample was dissolved with 2 molar equiv of aqueous sodium hydroxide (NaOH, 0.1 M) and then brought up to 5 mg/mL with distilled water. For preparation of the solutions of **A1**, PBI-DOPA was dissolved with 1 molar equiv of aqueous NaOH (0.1 M), and distilled water was added until the solutions reached 5 mg/mL.

Gelation of PBI-DOPA

Testing the gelation of the two solutions involved lowering the pH with 5 mg/mL GdL. GdL was added to the solution in 7 mL Sterlin cups. Samples were left overnight to gel. A simple vial inversion test was initially performed to indicate whether a gel had formed. If the sample was stable to inversion, then rheological studies were carried out.

Switching from H to J Aggregates

A solution of **A2** was converted to a solution of **A1** via the addition of 1 molar equiv of HCl (0.1 M). UV-vis absorption spectroscopy was then used to follow the formation of the aggregates of **A1**. This solution of **A1** could then be converted back to a solution of **A2** by the addition of 1 molar equiv of NaOH (0.1 M). Again, this was followed by UV-vis absorption spectroscopy.

Preparation of Samples on Glass Slides for Photoconductivity Measurements and Solid UV-Vis Measurements

Sample preparation involved dropping 10 μL of the required solution onto a glass microscope slide inside a 3 × 3 mm mask and then leaving the samples overnight to air dry. When the samples had dried, the mask could be removed, leaving a 3 × 3 mm square. Xerogel samples were prepared via the formation of gels as described above with GdL inside a 1 mL mold. Once gelation had occurred, the gel was then removed from the mold, and approximately 0.05 mL of the gel was removed with a scalpel, placed onto a glass microscope slide (again with a 3 × 3 mm mask), and allowed to air dry overnight. When the sample was dried, the mask could be removed, and two silver electrodes spaced 3 mm apart were then added. The silver electrodes were made with silver paste, which attached copper wires to the glass slide. Epoxy resin glue was placed over the silver electrodes. Again, this was left to dry overnight before measurements were performed.

Apparent pK_a Determination

For determining the apparent pK_a of each aggregate, a titration was performed. The pH of the two different solutions was measured, and the pH was slowly lowered by the addition of 5 μL of 0.1 HCl. An FC200 pH probe (HANNA instruments) with a 6 × 10 mm conical tip was used for pH measurements. The stated accuracy of the pH measurements is ±0.1. The temperature was maintained at 25°C during the titration with a circulating water bath. For apparent pK_a measurements, pH was recorded after each addition of HCl and a stable value was reached. For preventing the formation of a gel, the solutions were gently stirred with a stirrer bar so they would remain

liquid during the titration process. The plateaus of the pH indicate the two pK_a values of this gelator.

UV-Vis Absorption Spectroscopy

Solid and concentrated solution UV-vis absorption data were obtained with a Shimadzu UV-2550 UV-vis spectrophotometer running UV Probe software version 2.34. Solid samples were prepared as previously mentioned with GdL. This gel was then transferred onto a glass slide and allowed to air dry overnight to form a xerogel thin film. For solution UV-vis, the samples were prepared and transferred into a 0.1 mm quartz cuvette and allowed to gel overnight.

Dilution UV-vis absorption data were obtained with a Thermo Scientific Nanodrop 2000/2000c spectrophotometer. This was used in cuvette mode, and samples were prepared in 1 cm path length poly(methyl methacrylate) (PMMA) plastic cuvettes. Samples were diluted from 5 mg/mL with water at the same pH as the original samples.

SEM

SEM images were obtained with a Hitachi S-4800 FE-SEM. Gels and solutions at high pH were deposited onto glass coverslips, which were stuck onto aluminum SEM stubs by sticky carbon tabs and left to dry for 24 hr. Samples were measured in deceleration mode with an acceleration voltage between 1 and 3 kV at 3 mm.

Photoresponse Measurements

Photoresponse measurements were performed with an Autolab Potentiostat operating in a two-electrode configuration in the absence of a supporting electrolyte. Light supply was provided by 365, 400, 450, 470, 528, 590, and 628 nm LEDs (LZ1-10U600, LedEngin) with a light source powered by a TTi QL564P power supply operating at 3.9 V. Dark experiments were performed in an enclosure in air. Linear sweep measurements were recorded from −4 to 4 V at a scan rate of 0.05 V/s and a preconditioning step at 0.002 V for 2 s. The current recorded at 4 V was then used as the photoresponse value at each wavelength.

Rheological Measurements

Dynamic rheological and viscosity measurements were performed with an Anton Paar Physica MCR101 and MCR301 rheometer. A cup-and-vane measuring system was used for frequency and strain sweeps. A cone-and-plate measuring system was used for viscosity measurements and gelling under shear. A parallel-plate measuring system was used for time sweeps. For frequency and strain tests, 2 mL of the gels was prepared in 7 mL Sterilin vials and left for 24 hr at room temperature before the measurements were performed. For viscosity measurements, samples were prepared at high pH as previously mentioned. All experiments were performed at 25°C.

Frequency Sweep

Frequency scans were performed from 1 rad/s to 100 rad/s under a strain of 0.5%. The shear moduli (storage modulus [G′] and loss modulus [G″]) were read at 10 rad/s. These measurements were done within the viscoelastic region at which G′ and G″ were independent of strain amplitude.

Strain Sweep

Strain scans were performed from 0.1% to 1,000% with a frequency of 10 rad/s. The critical strain was quoted as the point at which G′ started to deviate for linearity and

ultimately crossed over the G″, resulting in gel breakdown. From these data, a strain of 0.5% used for measuring the frequency sweep was in the viscoelastic region.

Viscosity Measurements

Viscosity measurements were performed with a 50 mm cone and plate between 1 and 100 s^{-1}.

Fluorescence

Fluorescence spectra were recorded on a PerkinElmer Fluorescence Spectrometer LS55. Emission spectra were collected in 1.0 cm PMMA cuvettes. Samples were excited at 385 nm with a slit width of 5 nm at 100 nm/min. Samples were at a concentration of 0.05 mg/mL because this was the concentration at which both samples could be measured.

pXRD

Measurements were carried out on a Panalytical X'pert Pro multipurpose diffractometer with a Co Kα source (λ = 1.78 Å). Patterns were measured between 20 and 120° 2θ for 2 hr (step size 0.033°, time per step 295.3 s, and scan speed 0.014°/s).

Film Thickness

Film thickness was measured by atomic force microscopy. The tip was lowered until the slide was contacted, and the height was recorded. The tip was then lowered onto the sample, and the height was recorded once again. The difference in height was taken as the thickness of the sample. At least three measurements were carried out on each sample.

SANS

The solutions were prepared as described above but the H_2O and NaOH were replaced with D_2O and NaOD, respectively. The gels were prepared in UV-spectrophotometer-grade quartz cuvettes (Hellma) with a 2 mm path length. These were housed in a temperature-controlled sample rack during the measurements. SANS measurements were performed with the D11 instrument (Institut Laue-Langevin). A neutron beam with a fixed wavelength of 10 Å and divergence of $\Delta\lambda/\lambda$ = 9% allowed measurements over a large range for Q ($Q = 4\pi\sin(\theta/2)/\lambda$) of 0.001–0.3 $Å^{-1}$ by using three sample-detector distances of 1.4, 8, and 39 m.

The data were reduced to one-dimensional scattering curves of intensity versus Q with the software provided. The electronic background was subtracted, the full detector images for all data were normalized, and scattering from the empty cell was subtracted. The scattering from D_2O was also measured and subtracted from the data. Most of the data were radially averaged to produce the one-dimensional curves for each detector position. However, a number of the solutions at high pH, which were rich in 2NapFF, exhibited shear alignment on being pipetted into the cells. Hence, the data for these were split into sectors. The instrument-independent data were then fitted to the models discussed in the text with the SasView software package (http://sasview.org).

Time-Dependent DFT Calculations

The geometries of the different dimer models were optimized by dispersion-corrected DFT according to Grimme's PBEh-3c approach,[42] as implemented in Turbomole 7.01.[56] The vertical excitation spectra of the optimized dimer models were subsequently calculated with the long-range corrected wB97x[43] and CAM-B3LYP functionals[44] in Gaussian09[57] and GAMESS-US.[58] In both sets of calculations, the effect of the aqueous

environment in which the dimers and extended stacks reside was modeled with a dielectric screening model: the COSMO solvation model[59] and the PCM/SMD[60,61] solvation model, respectively. For more details, see the Supplemental Information.

SUPPLEMENTAL INFORMATION

Supplemental Information includes 14 figures, 3 tables, calculations, and DFT-optimized structures and excitation energies of the PDI-DOPA dimers and can be found with this article online at http://dx.doi.org/10.1016/j.chempr.2017.03.022.

AUTHOR CONTRIBUTIONS

Conceptualization, E.R.D and D.J.A.; Methodology, E.R.D., M.A.Z., R.S., and D.J.A.; Investigation, E.R.D., B.J.G M.B., M.A.Z., and D.J.A.; Writing, E.R.D., M.A.Z., and D.J.A.; Funding Acquisition, M.A.Z. and D.J.A.

ACKNOWLEDGMENTS

E.R.D. thanks the Engineering and Physical Sciences Research Council (EPSRC) for funding (EP/L021978/1), and M.Z. and D.A. thank the EPSRC for Fellowships (EP/I004424/1 and EP/L021978/1, respectively). M.B. thanks the UK Regenerative Medicine Platform for funding (MR/K026739/1). M.Z. acknowledges Dr. Kim Jelfs for assistance with the conformer searches and Dr. Gerrit-Jan Brandenburg for useful discussion. The experiment at the Institut Laue Langevin included allocated beam time under experiment number 9-11-1802 (DOI: 10.5291/ILL-DATA.9-11-1802). This work benefitted from the SasView software, originally developed by the DANSE project under National Science Foundation award DMR-0520547. Computational time on Archer, the UK's national high-performance computing service (via our membership of the UK's HPC Materials Chemistry Consortium, which is funded by EPSRC grant EP/L000202/1) is gratefully acknowledged. We thank Giulia Spennati (University of Glasgow) for the measurements of film thickness.

Received: November 22, 2016
Revised: February 21, 2017
Accepted: March 30, 2017
Published: May 11, 2017

REFERENCES AND NOTES

1. Moulin, E., Cid, J.-J., and Giuseppone, N. (2013). Advances in supramolecular electronics – from randomly self-assembled nanostructures to addressable self-organized interconnects. Adv. Mater. *25*, 477–487.

2. Korevaar, P.A., de Greef, T.F.A., and Meijer, E.W. (2014). Pathway complexity in π-conjugated materials. Chem. Mater. *26*, 576–586.

3. Praveen, V.K., Ranjith, C., and Armaroli, N. (2014). White-light-emitting supramolecular gels. Angew. Chem. Int. Ed. *53*, 365–368.

4. Jain, A., and George, S.J. (2015). New directions in supramolecular electronics. Mater. Today *18*, 206–214.

5. Hestand, N.J., and Spano, F.C. (2015). Interference between Coulombic and CT-mediated couplings in molecular aggregates: H- to J-aggregate transformation in perylene-based π-stacks. J. Chem. Phys. *143*, 244707.

6. Wurthner, F. (2004). Perylene bisimide dyes as versatile building blocks for functional supramolecular architectures. Chem. Commun. (Camb), 1564–1579, http://dx.doi.org/10.1039/B401630K.

7. Görl, D., Zhang, X., and Würthner, F. (2012). Molecular assemblies of perylene bisimide dyes in water. Angew. Chem. Int. Ed. *51*, 6328–6348.

8. Huang, C., Barlow, S., and Marder, S.R. (2011). Perylene-3,4,9,10-tetracarboxylic acid diimides: synthesis, physical properties, and use in organic electronics. J. Org. Chem. *76*, 2386–2407.

9. Chen, S., Slattum, P., Wang, C., and Zang, L. (2015). Self-assembly of perylene imide molecules into 1D nanostructures: methods, morphologies, and applications. Chem. Rev. *115*, 11967–11998.

10. Ghosh, S., Li, X.-Q., Stepanenko, V., and Würthner, F. (2008). Control of H- and J-type π stacking by peripheral alkyl chains and self-sorting phenomena in perylene bisimide Homo- and heteroaggregates. Chemistry *14*, 11343–11357.

11. Kaiser, T.E., Stepanenko, V., and Würthner, F. (2009). Fluorescent J-aggregates of core-substituted perylene bisimides: studies on structure–property relationship, nucleation–elongation mechanism, and sergeants-and-soldiers principle. J. Am. Chem. Soc. *131*, 6719–6732.

12. Jancy, B., and Asha, S.K. (2006). Control of molecular structure in the generation of highly luminescent liquid crystalline perylenebisimide derivatives: synthesis, liquid crystalline and photophysical properties. J. Phys. Chem. B *110*, 20937–20947.

13. Wu, H., Xue, L., Shi, Y., Chen, Y., and Li, X. (2011). Organogels based on J- and H-type aggregates of amphiphilic perylenetetracarboxylic diimides. Langmuir *27*, 3074–3082.

14. Sikdar, N., Dutta, D., Haldar, R., Ray, T., Hazra, A., Bhattacharyya, A.J., and Maji, T.K. (2016). Coordination-driven fluorescent J-aggregates in a perylenetetracarboxylate-based MOF: permanent porosity and proton conductivity. J. Phys. Chem. C *120*, 13622–13629.

15. Stoltzfus, D.M., Donaghey, J.E., Armin, A., Shaw, P.E., Burn, P.L., and Meredith, P. (2016). Charge generation pathways in organic solar cells: assessing the contribution from the electron acceptor. Chem. Rev. *116*, 12920–12955.

16. Tian, Y., Stepanenko, V., Kaiser, T.E., Wurthner, F., and Scheblykin, I.G. (2012). Reorganization of perylene bisimide J-aggregates: from delocalized collective to localized individual excitations. Nanoscale *4*, 218–223.

17. Marciniak, H., Li, X.-Q., Würthner, F., and Lochbrunner, S. (2011). One-dimensional exciton diffusion in perylene bisimide aggregates. J. Phys. Chem. A *115*, 648–654.

18. Lim, J.M., Kim, P., Yoon, M.-C., Sung, J., Dehm, V., Chen, Z., Wurthner, F., and Kim, D. (2013). Exciton delocalization and dynamics in helical π-stacks of self-assembled perylene bisimides. Chem. Sci. *4*, 388–397.

19. Yang, X., Xu, X., and Ji, H.-F. (2008). Solvent effect on the self-assembled structure of an amphiphilic perylene diimide derivative. J. Phys. Chem. B *112*, 7196–7202.

20. Yagai, S., Seki, T., Karatsu, T., Kitamura, A., and Würthner, F. (2008). Transformation from H- to J-aggregated perylene bisimide dyes by complexation with cyanurates. Angew. Chem. Int. Ed. *47*, 3367–3371.

21. Gregg, B.A., and Kose, M.E. (2008). Reversible switching between molecular and charge transfer phases in a liquid crystalline organic semiconductor. Chem. Mater. *20*, 5235–5239.

22. Sarbu, A., Biniek, L., Guenet, J.-M., Mesini, P.J., and Brinkmann, M. (2015). Reversible J- to H-aggregate transformation in thin films of a perylenebisimide organogelator. J. Mater. Chem. C *3*, 1235–1242.

23. Dwivedi, A.K., Pandeeswar, M., and Govindaraju, T. (2014). Assembly modulation of PDI derivative as a supramolecular fluorescence switching probe for detection of cationic surfactant and metal ions in aqueous media. ACS Appl. Mater. Interfaces *6*, 21369–21379.

24. Draper, E.R., Walsh, J.J., McDonald, T.O., Zwijnenburg, M.A., Cameron, P.J., Cowan, A.J., and Adams, D.J. (2014). Air-stable photoconductive films formed from perylene bisimide gelators. J. Mater. Chem. C *2*, 5570–5575.

25. Kozma, E., Grisci, G., Mróz, W., Catellani, M., Eckstein-Andicsovà, A., Pagano, K., and Galeotti, F. (2016). Water-soluble aminoacid functionalized perylene diimides: the effect of aggregation on the optical properties in organic and aqueous media. Dyes Pigm. *125*, 201–209.

26. Araujo, R.F., Silva, C.J.R., Paiva, M.C., Franco, M.M., and Proenca, M.F. (2013). Efficient dispersion of multi-walled carbon nanotubes in aqueous solution by non-covalent interaction with perylene bisimides. RSC Adv. *3*, 24535–24542.

27. Li, Y., Cheng, L., Liu, C., Xie, Y., Liu, W., Fan, Y., Li, X., and Fan, X. (2014). Hierarchical self-assembly of amino acid derivatives into stimuli-responsive luminescent gels. Soft Matter *10*, 8261–8266.

28. Ma, Y., Li, X., Wei, X., Jiang, T., Wu, J., and Ren, H. (2015). Synthesis and properties of amino acid functionalized water-soluble perylene diimides. Korean J. Chem. Eng. *32*, 1427–1433.

29. Kavery, E., Nagarajan, N., Paramaguru, G., and Renganathan, R. (2015). Synthesis, characterization and binding interactions of amino acids coupled perylene diimides with colloidal doped and undoped TiO2. Spectrochim. Acta A. Mol. Biomol. Spectrosc. *146*, 13–23.

30. Chal, P., Shit, A., and Nandi, A.K. (2016). Dye-sensitized solar cell from a new organic n-type semiconductor/polyaniline composite: insight from impedance spectroscopy. J. Mater. Chem. C *4*, 272–285.

31. Tuntiwechapikul, W., Taka, T., Béthencourt, M., Makonkawkeyoon, L., and Randall Lee, T. (2006). The influence of pH on the G-quadruplex binding selectivity of perylene derivatives. Bioorg. Med. Chem. Lett. *16*, 4120–4126.

32. Xu, Y., Leng, S., Xue, C., Sun, R., Pan, J., Ford, J., and Jin, S. (2007). A room-temperature liquid-crystalline phase with crystalline π stacks. Angew. Chem. Int. Ed. *46*, 3896–3899.

33. Chen, L., Revel, S., Morris, K., C Serpell, L., and Adams, D.J. (2010). Effect of molecular structure on the properties of naphthalene–dipeptide hydrogelators. Langmuir *26*, 13466–13471.

34. Tang, C., Smith, A.M., Collins, R.F., Ulijn, R.V., and Saiani, A. (2009). Fmoc-diphenylalanine self-assembly mechanism induces apparent pKa shifts. Langmuir *25*, 9447–9453.

35. Tang, C., Ulijn, R.V., and Saiani, A. (2013). Self-assembly and gelation properties of glycine/leucine Fmoc-dipeptides. Eur. Phys. J. E Soft Matter *36*, 111.

36. Würthner, F., Bauer, C., Stepanenko, V., and Yagai, S. (2008). A black perylene bisimide super gelator with an unexpected J-type absorption band. Adv. Mater. *20*, 1695–1698.

37. Kasha, M., Rawls, H.R., and Ashraf El-Bayoumi, M. (1965). The exciton model in molecular spectroscopy. Pure Appl. Chem. *11*, 371–392.

38. Casanova, D. (2015). Theoretical investigations of the perylene electronic structure: monomer, dimers, and excimers. Int. J. Quantum Chem. *115*, 442–452.

39. Zhao, H.-M., Pfister, J., Settels, V., Renz, M., Kaupp, M., Dehm, V.C., Würthner, F., Fink, R.F., and Engels, B. (2009). Understanding ground- and excited-state properties of perylene tetracarboxylic acid bisimide crystals by means of quantum chemical computations. J. Am. Chem. Soc. *131*, 15660–15668.

40. Settels, V., Liu, W., Pflaum, J., Fink, R.F., and Engels, B. (2012). Comparison of the electronic structure of different perylene-based dye-aggregates. J. Comput. Chem. *33*, 1544–1553.

41. Draper, E.R., Schweins, R., Akhtar, R., Groves, P., Chechik, V., Zwijnenburg, M.A., and Adams, D.J. (2016). Reversible photoreduction as a trigger for photoresponsive gels. Chem. Mater. *28*, 6336–6341.

42. Grimme, S., Brandenburg, J.G., Bannwarth, C., and Hansen, A. (2015). Consistent structures and interactions by density functional theory with small atomic orbital basis sets. J. Chem. Phys. *143*, 054107.

43. Chai, J.-D., and Head-Gordon, M. (2008). Systematic optimization of long-range corrected hybrid density functionals. J. Chem. Phys. *128*, 084106.

44. Yanai, T., Tew, D.P., and Handy, N.C. (2004). A new hybrid exchange–correlation functional using the Coulomb-attenuating method (CAM-B3LYP). Chem. Phys. Lett. *393*, 51–57.

45. Pocker, Y., and Green, E. (1973). Hydrolysis of D-glucono-.delta.-lactone. I. General acid-base catalysis, solvent deuterium isotope effects, and transition state characterization. J. Am. Chem. Soc. *95*, 113–119.

46. Adams, D.J., Butler, M.F., Frith, W.J., Kirkland, M., Mullen, L., and Sanderson, P. (2009). A new method for maintaining homogeneity during liquid-hydrogel transitions using low molecular weight hydrogelators. Soft Matter *5*, 1856–1862.

47. Draper, E.R., Mykhaylyk, O.O., and Adams, D.J. (2016). Aligning self-assembled gelators by drying under shear. Chem. Commun. *52*, 6934–6937.

48. Walsh, J.J., Lee, J.R., Draper, E.R., King, S.M., Jäckel, F., Zwijnenburg, M.A., Adams, D.J., and Cowan, A.J. (2016). Controlling visible light driven photoconductivity in self-assembled perylene bisimide structures. J. Phys. Chem. C *120*, 18479–18486.

49. Draper, E.R., Lee, J.R., Wallace, M., Jackel, F., Cowan, A.J., and Adams, D.J. (2016). Self-sorted photoconductive xerogels. Chem. Sci. *7*, 6499–6505.

50. Marcon, R.O., and Brochsztain, S. (2009). Aggregation of 3,4,9,10-perylenediimide radical anions and dianions generated by reduction with dithionite in aqueous solutions. J. Phys. Chem. A *113*, 1747–1752.

51. Roy, S., Kumar Maiti, D., Panigrahi, S., Basak, D., and Banerjee, A. (2012). A new hydrogel from an amino acid-based perylene bisimide and its semiconducting, photo-switching behaviour. RSC Adv. *2*, 11053–11060.

52. Wu, N., Wang, C., Slattum, P.M., Zhang, Y., Yang, X., and Zang, L. (2016). Persistent photoconductivity in perylene diimide nanofiber materials. ACS Energy Lett. *1*, 906–912.

53. Russ, B., Robb, M.J., Popere, B.C., Perry, E.E., Mai, C.-K., Fronk, S.L., Patel, S.N., Mates, T.E., Bazan, G.C., Urban, J.J., et al. (2016). Tethered tertiary amines as solid-state n-type dopants for solution-processable organic semiconductors. Chem. Sci. *7*, 1914–1919.

54. Russ, B., Robb, M.J., Brunetti, F.G., Miller, P.L., Perry, E.E., Patel, S.N., Ho, V., Chang, W.B.,

Urban, J.J., Chabinyc, M.L., et al. (2014). Power factor enhancement in solution-processed organic n-type thermoelectrics through molecular design. Adv. Mater. *26*, 3473–3477.

55. Raeburn, J., Zamith Cardoso, A., and Adams, D.J. (2013). The importance of the self-assembly process to control mechanical properties of low molecular weight hydrogels. Chem. Soc. Rev. *42*, 5143–5156.

56. Furche, F., Ahlrichs, R., Hättig, C., Klopper, W., Sierka, M., and Weigend, F. (2014). Turbomole. Wiley Interdiscip. Rev. Comput. Mol. Sci. *4*, 91–100.

57. Frisch, M.J., Trucks, G.W., Schlegel, H.B., Scuseria, G.E., Robb, M.A., Cheeseman, J.R., Scalmani, G., Barone, V., Petersson, G.A., Nakatsuji, H., et al. (2016). Gaussian 09, Revision C.01 (Gaussian, Inc.).

58. Schmidt, M.W., Baldridge, K.K., Boatz, J.A., Elbert, S.T., Gordon, M.S., Jensen, J.H., Koseki, S., Matsunaga, N., Nguyen, K.A., Su, S., et al. (1993). General atomic and molecular electronic structure system. J. Comput. Chem. *14*, 1347–1363.

59. Klamt, A., and Schuurmann, G. (1993). COSMO: a new approach to dielectric screening in solvents with explicit expressions for the screening energy and its gradient. J. Chem. Soc. Perkin Trans. 2, 799–805, http://dx.doi.org/10.1039/P29930000799.

60. Miertuš, S., Scrocco, E., and Tomasi, J. (1981). Electrostatic interaction of a solute with a continuum. A direct utilization of AB initio molecular potentials for the prevision of solvent effects. Chem. Phys. *55*, 117–129.

61. Marenich, A.V., Cramer, C.J., and Truhlar, D.G. (2009). Universal solvation model based on solute electron density and on a continuum model of the solvent defined by the bulk dielectric constant and atomic surface tensions. J. Phys. Chem. B *113*, 6378–6396.